


# Suppression of the Kelvin-Helmholtz instability by coating in the double-cone ignition scheme

Yuan-Kai Xie(谢元凯), Cheng-Long Zhang(张成龙), Yi-Zhen Cheng(程翊真), and Ying-Jun Li(李英骏)

**Citation:**Chin. Phys. B, 2024, 33 (**12**): 125203. DOI: 10.1088/1674-1056/ad8551
Journal homepage: http://cpb.iphy.ac.cn; http://iopscience.iop.org/cpb

**What follows is a list of articles you may be interested in**

---

## Plasma potential measurements using an emissive probe made of oxide cathode

Jian-Quan Li(李建泉), Hai-Jie Ma(马海杰), and Wen-Qi Lu(陆文琪)
Chin. Phys. B, 2024, 33 (**4**): 045205. DOI: 10.1088/1674-1056/ad1821

## Preparation of Se-based solar cell using spin-coating method in ambient condition

Menghua Zhu(朱孟花), Yaxin Deng(邓雅心), Weiwei Liu(刘伟伟), Xin Li(李欣)
Chin. Phys. B, 2018, 27 (**1**): 015202. DOI: 10.1088/1674-1056/27/1/015202

## Characteristics of helium DC plasma jets at atmospheric pressure with multiple cathodes

Cheng Wang(王城), Zelong Zhang(张泽龙), Haichao Cui(崔海超), Weiluo Xia(夏维珞), Weidong Xia(夏维东)
Chin. Phys. B, 2017, 26 (**8**): 085207. DOI: 10.1088/1674-1056/26/8/085207

## Effect of deposition parameters on structural and mechanicalproperties of niobium nitride synthesized by plasma focus device

Jamil Siddiqui, Tousif Hussain, Riaz Ahmad, Nida Khalid
Chin. Phys. B, 2015, 24 (**6**): 065204. DOI: 10.1088/1674-1056/24/6/065204

## Preparation of biomedical Ag incorporated hydroxyapatite/titania coatings on Ti6Al4V alloy by plasma electrolytic oxidation

Zhou Lan (周澜), Lü Guo-Hua (吕国华), Mao Fei-Fei (毛菲菲), Yang Si-Ze (杨思泽)
Chin. Phys. B, 2014, 23 (**3**): 035205. DOI: 10.1088/1674-1056/23/3/035205

---

# Suppression of the Kelvin–Helmholtz instability by coating in the double-cone ignition scheme

Yuan-Kai Xie(谢元凯)[1,2], Cheng-Long Zhang(张成龙)[2], Yi-Zhen Cheng(程翊真)[1,2], and Ying-Jun Li(李英骏)[2,†]

[1] *School of Science, China University of Mining and Technology, Beijing* 100083, *China*

[2] *State Key Laboratory for Tunnel Engineering, China University of Mining and Technology, Beijing* 100083, *China*

(Received 30 July 2024; revised manuscript received 9 September 2024; accepted manuscript online 10 October 2024)

In order to address the issue of gold mixing caused by the Kelvin–Helmholtz instability (KHI) in the double-cone ignition (DCI) scheme, we investigate the growth rate of the KHI at the bi-interface of the DCI scheme after applying a coating. This is done by solving the hydrodynamic equations for an ideal incompressible fluid using linear theory. Ultimately, it is discovered that applying a coating with a thickness slightly above $h = 0.5(\lambda + 10\ \mu\text{m})$ and a density somewhat lower than that of the target layer can effectively reduce the growth rate of interfacial KHI. This work provides theoretical references for studying the bi-interface KHI in the DCI scheme.

**Keywords:** coating, Kelvin–Helmholtz instability, double-cone ignition scheme, growth rate

**PACS:** 52.57.–z, 52.30.Ex, 47.20.Ft **DOI:** 10.1088/1674-1056/ad8551

## 1. Introduction

The Kelvin–Helmholtz instability (KHI)[1–3] arises from the relative motion of fluid layers having disparate velocities near an interface. The fluid instability model is applicable for the study of various types of fluids, including compressible fluids,[4] incompressible fluids[5] and fluids subjected to a magnetic field.[6] In 2020, Zhang *et al.*[7] introduced a novel double-cone ignition (DCI) scheme that combines the benefits of fast[8–11] and conventional ignition methods. When a high-energy laser beam is directed at a fusion target, the liquid layer on the target's surface undergoes intense compression and generates a rapid flow along the walls of the gold cone.[12] Shear forces are generated at the interface due to the disparate velocities of the fuel target layer and the gold cone layer. The KHI generates vortices and ripples at the boundary of fluids, which initiate the mixing and dispersion of the layers of fluid with different velocities. This process ultimately results in the blending of the fuel and gold plasma at the opening of the cone. This impacts the efficiency of the ignition and the stability of the energy output, hence diminishing its potential for achieving successful fusion.

In recent decades, research on inertial confinement fusion[13–26] has never stopped. Although there has been a lot of research[27–32] on the DCI scheme since it was proposed by Zhang and Hu in 2020, few people have systematically explored the gold mixing problem caused by KHI. Zhang *et al.*[28] discovered that coating a layer of DT fuel between the gold cone and the target fuel layer could effectively reduce the non-centripetal kinetic energy caused by KHI rolling-up. However, that study simply established that increasing the coating has a positive impact on preventing gold mixing. It did not provide explicit instructions on how to coat it to get optimal results based on the theoretical mechanism. Using linear theory, this paper thoroughly examines the quantitative correlation between certain physical characteristics of the intermediate coating and the growth rate of KHI. Ultimately, a specific DCI coating scheme is proposed to effectively mitigate the damage caused to ignition by KHI.

This paper is organized as follows. In Section 2, we derive the theoretical model and verify its correctness and applicability; in Section 3 we analyze and discuss the numerical simulation results obtained using the equations; finally, in Section 4, the conclusions are summarized.

## 2. Theoretical modeling and validation

Since the interface changes from the original single interface to a bi-interface after the DCI scheme is coated, we can replace the gold cone, the coating layer and the fuel target layer with three material layers of different densities, as shown schematically in Fig. 1.

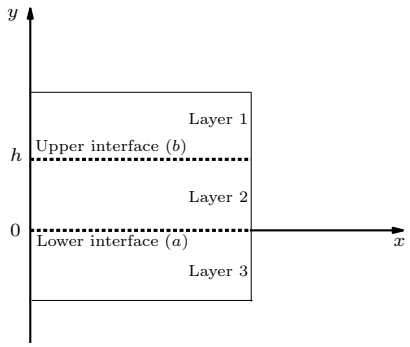



**Fig. 1.** Schematic diagram of a bi-interfacial fluid.

†Corresponding author. E-mail: lyj@aphy.iphy.ac.cn

© 2024 Chinese Physical Society and IOP Publishing Ltd 

The density of this finite-thickness fluid layer is $\rho_2$, and the thickness is $h$. Since the coating layer is very thin compared with the cone layer and target layer, we regard both the cone layer and target layer as semi-infinite fluid layers with densities of $\rho_1$ and $\rho_3$, respectively. We assume that the interface experiences an irrotational perturbation perpendicular to it. The lower interface is denoted by $a$ $(y=\eta_a(x,t))$ and the upper interface is denoted by $b$ $(y=h+\eta_b(x,t))$, where $\eta_i(x,t)$ represents the small displacement perturbation along the $y$ direction at interface $i$. At the initial moment, the interface perturbation $\eta(x,t=0)=\varepsilon\cos kx$ is introduced, where $\varepsilon$ represents the initial perturbation amplitude and $k$ denotes the perturbation wave number. The flow velocity difference exists during the flow of the fluid layer along the interface direction, denoted by $u_1$, $u_2$ and $u_3$, respectively.

From the hydrodynamic equations of an incompressible[5] ideal fluid in the absence of a gravitational field, we have

$$\frac{\partial\rho}{\partial t}+\nabla\cdot(\rho\boldsymbol{u})=0,\quad \frac{\partial\boldsymbol{u}}{\partial t}+(\boldsymbol{u}\cdot\nabla)\boldsymbol{u}+\frac{\nabla p}{\rho}=0, \tag{1}$$

where $\rho$, $p$, $\boldsymbol{u}$ and $t$ are the density, pressure, velocity and time, respectively. For an irrotational fluid, we can introduce the velocity potential $\Phi$, which satisfies the condition $\boldsymbol{u}=\nabla\Phi$. Each of the three fluid layers has a finite velocity $u_i$ $(i=1,2,3)$ in the $x$ direction. Neglecting the potential field, let the velocity potential be $\Phi_i=u_i x+\varphi_i(x,t)$, where $\varphi_i$ is the perturbation velocity potential. Substituting the speed potential $\Phi$ into the normal velocity continuity condition $u_{1\mathrm{n}}=u_{2\mathrm{n}}$ and the pressure continuity condition $p_1=p_2$, then expanding them at $y=h$ based on the Taylor series, we obtain

$$\begin{aligned}
&-\eta_{bx}(u_1+\varphi_{1x})+\varphi_{1y}+\varphi_{1yy}\eta_b\Big|_{y=h}\\
=\;&-\eta_{bx}(u_2+\varphi_{2x})+\varphi_{2y}+\varphi_{2yy}\eta_b\Big|_{y=h}, \qquad (2)\\
&\rho_1\Big\{\Phi_{1t}+\Phi_{1ty}\eta_b+u_1\varphi_{1x}+u_1\varphi_{1xy}\eta_b\\
&+\frac{1}{2}(u_1^2+\varphi_{1x}^2+\varphi_{1y}^2)-f_1(t)\Big\}\Big|_{y=h}\\
=\;&\rho_2\Big\{\Phi_{2t}+\Phi_{2ty}\eta_b+u_2\varphi_{2x}+u_2\varphi_{2xy}\eta_b\\
&+\frac{1}{2}(u_2^2+\varphi_{2x}^2+\varphi_{2y}^2)-f_2(t)\Big\}\Big|_{y=h}. \qquad (3)
\end{aligned}$$

Here $f_i(t)$ is an integral function that depends only on time $t$. Assuming that the initial perturbation amplitude $\varepsilon$ is much smaller than the perturbation wavelength, perturbative expansions of the interface displacement $\eta_b$ and the perturbation velocity potential $\varphi_i$ $(i=1,2)$ are

$$\begin{aligned}
\varphi_i&=\varepsilon\varphi_i^{(1)}+\varepsilon^2\varphi_i^{(2)}+O(\varepsilon^3),\\
\eta_b&=h+\varepsilon\eta_b^{(1)}+\varepsilon^2\eta_b^{(2)}+O(\varepsilon^3).
\end{aligned} \tag{4}$$

These rank terms are matched with the boundary conditions (2) and (3). The multi-order terms give weakly nonlinear corrections, so we will only look at the first-order linear solutions here. The two boundary conditions thus become first-order quantitative equations as follows:

$$\eta^{(1)}{}_{bt}=\varphi_{1y}^{(1)}\big|_{y=h}-u_1\eta^{(1)}{}_{bx}=\varphi_{2y}^{(1)}\big|_{y=h}-u_2\eta^{(1)}{}_{bx}, \tag{5}$$

$$\rho_1\big(\varphi_{1t}^{(1)}\big|_{y=h}+u_1\varphi_{1x}^{(1)}\big)=\rho_2\big(\varphi_{2t}^{(1)}\big|_{y=h}+u_2\varphi_{2x}^{(1)}\big). \tag{6}$$

Since the fluid is an incompressible, irrotational ideal fluid, the velocity potential must satisfy the Laplace equation $\nabla^2\Phi=0$. We can set

$$\begin{aligned}
\varphi_1&=\left[a(t)\,\mathrm{e}^{\mathrm{i}kx}+a^*(t)\,\mathrm{e}^{-\mathrm{i}kx}\right]\mathrm{e}^{-ky},\\
\varphi_2&=\left[b(t)\,\mathrm{e}^{\mathrm{i}kx}+b^*(t)\,\mathrm{e}^{-\mathrm{i}kx}\right]\mathrm{e}^{ky}\\
&\quad+\left[c(t)\,\mathrm{e}^{\mathrm{i}kx}+c^*(t)\,\mathrm{e}^{-\mathrm{i}kx}\right]\mathrm{e}^{-ky},\\
\varphi_3&=\left[d(t)\,\mathrm{e}^{\mathrm{i}kx}+d^*(t)\,\mathrm{e}^{-\mathrm{i}kx}\right]\mathrm{e}^{ky},
\end{aligned} \tag{7}$$

where $k$ represents the disturbance wave number while $\varphi_1$, $\varphi_2$ and $\varphi_3$ denote the disturbance velocity potential in the three fluid layers. $a(t)$, $b(t)$, $c(t)$ and $d(t)$ are temporal functions.

By substituting $\varphi_1$ and $\varphi_2$ into the first-order quantitative equations and replacing $\eta_b$ with $\eta_b\,\mathrm{e}^{\mathrm{i}kx}+\eta_b^*\,\mathrm{e}^{-\mathrm{i}kx}$ to ease the separation of variables, we derive

$$\begin{aligned}
&\eta_{bt}\,\mathrm{e}^{\mathrm{i}kx}+\eta_{bt}^*\,\mathrm{e}^{-\mathrm{i}kx}\\
=\;&-k[a(t)\,\mathrm{e}^{\mathrm{i}kx}+a^*(t)\,\mathrm{e}^{-\mathrm{i}kx}]\,\mathrm{e}^{-kh}-\mathrm{i}ku_1(\eta_b\,\mathrm{e}^{\mathrm{i}kx}-\eta_b^*\,\mathrm{e}^{-\mathrm{i}kx}),\\
&\eta_{bt}\,\mathrm{e}^{\mathrm{i}kx}+\eta_{bt}^*\,\mathrm{e}^{-\mathrm{i}kx}\\
=\;&k[b(t)\,\mathrm{e}^{\mathrm{i}kx}+b^*(t)\,\mathrm{e}^{-\mathrm{i}kx}]\,\mathrm{e}^{kh}\\
&-k[c(t)\,\mathrm{e}^{\mathrm{i}kx}+c^*(t)\,\mathrm{e}^{-\mathrm{i}kx}]\,\mathrm{e}^{-kh}-\mathrm{i}ku_2(\eta_b\,\mathrm{e}^{\mathrm{i}kx}-\eta_b^*\,\mathrm{e}^{-\mathrm{i}kx}),
\end{aligned} \tag{8}$$

$$\begin{aligned}
&\rho_1\big[(a_t(t)\,\mathrm{e}^{\mathrm{i}kx}+a_t^*(t)\,\mathrm{e}^{-\mathrm{i}kx})\,\mathrm{e}^{-kh}\\
&+\mathrm{i}ku_1(a(t)\,\mathrm{e}^{\mathrm{i}kx}-a^*(t)\,\mathrm{e}^{-\mathrm{i}kx})\,\mathrm{e}^{-kh}\big]\\
=\;&\rho_2\big\{\big[(b_t(t)\,\mathrm{e}^{\mathrm{i}kx}+b_t^*(t)\,\mathrm{e}^{-\mathrm{i}kx})\,\mathrm{e}^{kh}\\
&+(c_t(t)\,\mathrm{e}^{\mathrm{i}kx}+c_t^*(t)\,\mathrm{e}^{-\mathrm{i}kx})\,\mathrm{e}^{-kh}\big]\\
&+\mathrm{i}ku_2\big[(b_t(t)\,\mathrm{e}^{\mathrm{i}kx}-b_t^*(t)\,\mathrm{e}^{-\mathrm{i}kx})\,\mathrm{e}^{kh}\\
&+(c_t(t)\,\mathrm{e}^{\mathrm{i}kx}-c_t^*(t)\,\mathrm{e}^{-\mathrm{i}kx})\,\mathrm{e}^{-kh}\big]\big\}.
\end{aligned} \tag{9}$$

We separate the variables to obtain two sets of equations. The first set of equations is

$$\begin{aligned}
&\rho_1[a_t(t)+\mathrm{i}ku_1a(t)]\,\mathrm{e}^{-kh}\\
=\;&\rho_2[b_t(t)+\mathrm{i}ku_2b(t)]\,\mathrm{e}^{kh}+\rho_2[c_t(t)+\mathrm{i}ku_2c(t)]\,\mathrm{e}^{-kh},\\
&\eta_{bt}=-ka(t)\,\mathrm{e}^{-kh}-\mathrm{i}ku_1\eta_b,\\
&\eta_{bt}=kb(t)\,\mathrm{e}^{kh}-kc(t)\,\mathrm{e}^{-kh}-\mathrm{i}ku_2\eta_b.
\end{aligned} \tag{10}$$

The second set of equations is

$$\begin{aligned}
&\rho_1a_t^*(t)\,\mathrm{e}^{-kh}-\rho_1\mathrm{i}ku_1a_t^*(t)\,\mathrm{e}^{-kh}\\
=\;&\rho_2[b_t^*(t)-\mathrm{i}ku_2b^*(t)]\,\mathrm{e}^{kh}+\rho_2[c_t^*(t)-\mathrm{i}ku_2c^*(t)]\,\mathrm{e}^{-kh},\\
&\eta_{bt}^*=-ka^*(t)\,\mathrm{e}^{-kh}+\mathrm{i}ku_1\eta_b,
\end{aligned}$$

$$\eta_{bt}^{*} = kb^{*}(t)\,\mathrm{e}^{kh} - kc^{*}(t)\,\mathrm{e}^{-kh} + \mathrm{i}ku_2\eta_b. \tag{11}$$

By taking the conjugate of both sides of the first set of equations, we may derive the second set, thus reducing the problem to solving only the first set. Similarly, we can obtain two sets of conjugate-equalizable equations concerning the lower interface $a$. The first set of equations is

$$\begin{aligned} &\rho_2[b_t(t) + \mathrm{i}ku_2 b(t)] + \rho_2[c_t(t) + \mathrm{i}ku_2 c(t)] \\ &= \rho_3[d_t(t) + \mathrm{i}ku_3 d(t)], \\ &\eta_{at} = kd(t) - \mathrm{i}ku_3\eta_a, \\ &\eta_{at} = k(b(t) - c(t)) - \mathrm{i}ku_2\eta_a. \end{aligned} \tag{12}$$

The second set of equations is

$$\begin{aligned} &\rho_2[b_t^{*}(t) - \mathrm{i}ku_2 b^{*}(t)] + \rho_2[c_t^{*}(t) - \mathrm{i}ku_2 c^{*}(t)] \\ &= \rho_3[d_t^{*}(t) + \mathrm{i}ku_3 d^{*}(t)], \\ &\eta_{at}^{*} = kd^{*}(t) + \mathrm{i}ku_3\eta_a^{*}, \\ &\eta_{at}^{*} = k(b^{*}(t) - c^{*}(t)) + \mathrm{i}ku_2\eta_a^{*}. \end{aligned} \tag{13}$$

Let us combine Eqs. (10) and (12). From the fact that the linear time factor $\chi = \gamma - \mathrm{i}\omega$ satisfies the fluctuation form $\mathrm{e}^{\mathrm{i}kx+\chi t}$, it follows that the time-inclusive function satisfies $A_t = \chi A$. We have

$$\begin{cases} \rho_1 a(t)(\chi + \rho_1 \mathrm{i}ku_1)\,\mathrm{e}^{-kh} \\ = \rho_2 b(t)[\chi + \mathrm{i}ku_2]\,\mathrm{e}^{kh} + \rho_2 c(t)[\chi + \mathrm{i}ku_2]\,\mathrm{e}^{-kh}, \\ \rho_2 b(t)[\chi + \mathrm{i}ku_2] + \rho_2 c(t)[\chi + \mathrm{i}ku_2] = \rho_3 d(t)[\chi + \mathrm{i}ku_3], \\ (\chi + \mathrm{i}ku_1)\eta_b = -ka(t)\,\mathrm{e}^{-kh}, \\ (\chi + \mathrm{i}ku_2)\eta_b = kb(t)\,\mathrm{e}^{kh} - kc(t)\,\mathrm{e}^{-kh}, \\ (\chi + \mathrm{i}ku_3)\eta_a = kd(t), \\ (\chi + \mathrm{i}ku_2)\eta_a = k(b(t) - c(t)). \end{cases} \tag{14}$$

The combined solution results in a system of binary equations with variables $b(t)$ and $c(t)$:

$$\begin{aligned} &b(t)[\rho_2(\chi + \mathrm{i}ku_2)^2 + \rho_1(\chi + \mathrm{i}ku_1)^2]\,\mathrm{e}^{2kh} \\ &+ c(t)[\rho_2(\chi + \mathrm{i}ku_2)^2 - \rho_1(\chi + \mathrm{i}ku_1)^2] = 0, \\ &b(t)[\rho_2(\chi + \mathrm{i}ku_2)^2 - \rho_3(\chi + \mathrm{i}ku_3)^2] \\ &+ c(t)[\rho_2(\chi + \mathrm{i}ku_2)^2 + \rho_3(\chi + \mathrm{i}ku_3)^2] = 0. \end{aligned} \tag{15}$$

The condition for the existence of a solution in a system of equations is that the determinant of the coefficient matrix must be equal to zero. Therefore, we can finally derive a one-dimensional quartic equation on $\chi$:

$$\begin{aligned} &[\rho_2(\chi + \mathrm{i}ku_2)^2 + \rho_3(\chi + \mathrm{i}ku_3)^2] \\ &\times [\rho_2(\chi + \mathrm{i}ku_2)^2 + \rho_1(\chi + \mathrm{i}ku_1)^2]\,\mathrm{e}^{2kh} \\ &+ [\rho_1(\chi + \mathrm{i}ku_1)^2 - \rho_2(\chi + \mathrm{i}ku_2)^2] \\ &\times [\rho_2(\chi + \mathrm{i}ku_2)^2 - \rho_3(\chi + \mathrm{i}ku_3)^2] = 0. \end{aligned} \tag{16}$$

When the thickness of the middle finite-thickness layer, $h$, approaches zero, a bi-interface fluid can be approximated as a single-interface fluid. The linear growth rate obtained at this time should be consistent with the classical linear growth rate under a single interface:

$$\gamma = \sqrt{k^2 \frac{\rho_a\rho_b(u_a - u_b)^2}{(\rho_a + \rho_b)^2}}. \tag{17}$$

As the thickness of the middle layer $h$ approaches infinity, the upper and lower interfaces become completely independent and do not interact with each other. Examination of the upper and lower interfaces can be conducted through utilization of the single-interface linear and weakly nonlinear theories. The two growth rates determined independently in the linear scenario should also align with Eq. (17). Due to the dominance of the growing portion over the weakening part in fluid instability, our analysis focuses solely on the two positive solutions $\chi_1$ and $\chi_2$. We then extract their real parts to obtain the linear growth rates $\gamma_1$ and $\gamma_2$. As the limit of $h$ approach $\theta$, Eq. (16) can be modified to

$$\begin{aligned} &[\rho_1(\chi + \mathrm{i}ku_1)^2 - \rho_2\chi^2][\rho_2\chi^2 - \rho_3(\chi + \mathrm{i}ku_3)^2] \\ &+ [\rho_2\chi^2 + \rho_3(\chi + \mathrm{i}ku_3)^2][\rho_1(\chi + \mathrm{i}ku_1)^2 + \rho_2\chi^2] = 0. \end{aligned} \tag{18}$$

By simplifying and solving Eq. (18) and considering only its real element, the linear growth rate can be obtained as

$$\gamma = \sqrt{k^2 \frac{\rho_1\rho_3\,(u_1 - u_3)^2}{(\rho_1 + \rho_3)^2}}. \tag{19}$$

As $h$ tends to infinity, Eq. (16) can be changed to

$$\begin{aligned} &[\rho_2(\chi + \mathrm{i}ku_2)^2 + \rho_3(\chi + \mathrm{i}ku_3)^2] \\ &\times [\rho_2(\chi + \mathrm{i}ku_2)^2 + \rho_1(\chi + \mathrm{i}ku_1)^2] = 0. \end{aligned} \tag{20}$$

Simplifying to solve Eq. (20) and taking its real part respectively, one gets

$$\gamma = \sqrt{k^2 \frac{\rho_1\rho_2\,(u_1 - u_2)^2}{(\rho_1 + \rho_2)^2}}, \quad \gamma = \sqrt{k^2 \frac{\rho_2\rho_3\,(u_2 - u_3)^2}{(\rho_2 + \rho_3)^2}}. \tag{21}$$

It can be seen that the three linear growth rates are consistent with Eq. (17), so we have validated the correctness of Eq. (16). Next, let us use an example to prove the applicability of Eq. (16) in exploring growth rate suppression. We first calculate the single-interface growth rate without coating, then numerically simulate the growth rate after adding coating by equation, and finally compare the results before and after.

Let us first investigate the uncoated case. The density of gold is $\rho_1 = 19.3$ g·cm$^3$, and the density of CHCl is $\rho_3 = 1.48$ g·cm$^3$. The perturbation wavelength is 40 μm, taking $u_1 = 0$ and $u_3 = 40$ μm·ns$^{-1}$. Using the single-interface equation $\gamma = (1/2)k|\Delta u|\sqrt{1 - A^2}$, the single-interface growth rate $\gamma_{\mathrm{Au-CHCl}}$ can be calculated separately for different perturbation wavelengths from 10 μm to 70 μm.

After calculating the growth rates of the single interface at different wavelengths before coating, we then start to coat between Au and CHCl. For the convenience of the study, and to reduce the number of unknowns studied, we divide both sides of Eq. (16) by $\rho_3$, regard $\rho_2/\rho_3$ as a whole, write as $\rho_{23}$ and then write $\rho_1/\rho_3$ as $\rho_{13}$. A quartic equation about $\chi$ can be obtained as

$$\begin{aligned}&[\rho_{23}(\chi+\mathrm{i}ku_2)^2+(\chi+\mathrm{i}ku_3)^2]\\&\times[\rho_{23}(\chi+\mathrm{i}ku_2)^2+\rho_{13}(\chi+\mathrm{i}ku_1)^2]\mathrm{e}^{2kh}\\&+[\rho_{13}(\chi+\mathrm{i}ku_1)^2-\rho_{23}(\chi+\mathrm{i}ku_2)^2]\\&\times[\rho_{23}(\chi+\mathrm{i}ku_2)^2-(\chi+\mathrm{i}ku_3)^2]=0.\end{aligned}\tag{22}$$

Because gold has a very high density, its fluid velocity is very low. Furthermore, the velocity difference directly influences the KHI. We can take the gold cone flow velocity as approximately $u_1=0$. After adding a thickness $h=5$ μm and density $\rho_2=0.9$ g·cm$^3$ for the coated CH, the density ratio $\rho_{13}=13.0405$ and $\rho_{23}=0.6081$. We take $u_2=35$ μm·ns$^{-1}$, and take different values of the perturbation wavelength from 10 μm to 70 μm. We substitute all the above-given conditions into Eq. (22) and take the real part of the two positive solutions to obtain the growth rates of the two interfaces. It is worth noting that we take the real parts of the two positive solutions to correspond to the instability growth rates of the two interfaces, which actually employs a simplified equivalent concept. Due to the finite thickness of the coating and the coupling of all three velocity perturbations in Eq. (22), the perturbation eigenmodes corresponding to the two growth rates will be influenced by coupling effects. As a result, the perturbation eigenmodes are expected to be distributed across all regions of the entire system rather than being confined solely to the two interfaces. Therefore, as long as the growth rates at the two interfaces that we equate can essentially yield the final system growth rate, we choose to ideally equate these regionally distributed perturbation eigenmodes at the two most representative interfaces.

We have plotted the above two sets of data against each other. The growth rates of the Au–CHCl, Au–CH and CH–CHCl interfaces at different wavelengths with the addition of the coating layer are shown in Fig. 2.

The comparison graph reveals that the addition of the coating reduced the KHI growth rate at the gold cone wall interface at any wavelength, resulting in a growth rate at both interfaces that was lower than that without the coating. This shows that the probability that Au enters the CHCl layer and the cone mouth through the rolling-up effect becomes smaller, weakening the effect on the target layer's fuel. This result is consistent with the conclusion of Zhang *et al*. It is also an applicable proof of using the quartic equation in one dimension to investigate the KHI growth rate.

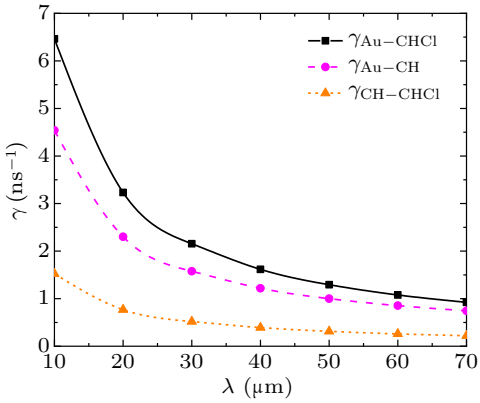



**Fig. 2.** Variation of KHI growth rate before and after adding coatings at different wavelengths.

## 3. Research and results

### 3.1. Pre-research analyses

We can see that the four conditions — the material's thickness $h$, its density $\rho$, its flow velocity $u$ and the wave number $k$ of the perturbation wavelength — all have an effect on the change in the growth rate that we are studying. However, during the actual model construction process, we struggle to easily and accurately control the material flow rate and the perturbation wavelength. As a result, this paper focuses on the effectiveness of various coating thickness and density conditions in suppressing the KHI growth rate in the DCI scheme.

As the focus of this paper is the impact of the coating layer added between the gold cone and the target layer, we do not consider the density change of the gold cone and the target layer material. So $\rho_1$ and $\rho_3$ are regarded as two certain values. Considering the density characteristics of different materials, the density of gold varies from 10 to 20 times that of the target layer materials CH, CD, CHCl and so on. To simplify the study, we use an average value of 15. That is $\rho_{13}=15$ and remains constant.

### 3.2. Effect of coating thickness on growth rate

Firstly, to investigate the effect of coating thickness on growth rate, we study the variation of KHI growth rate with thickness at three perturbation wavelengths. The density conditions are adopted as $\rho_{13}=15$ and $\rho_{23}=0.9$. The velocity conditions are set as $u_1=0$, $u_2=20$ μm·ns$^{-1}$, and $u_3=40$ μm·ns$^{-1}$. The three simulation environments of the perturbation wavelengths are adopted as $\lambda=20$ μm, $\lambda=30$ μm and $\lambda=40$ μm, respectively.

A graph of the growth rate versus thickness for the three wavelength environments is shown in Fig. 3. From the graph, we can indeed see that when the coating layer reaches a certain thickness, the growth rate remains constant at a certain value, no matter how large the thickness becomes. We refer to this as the critical saturation thickness. In the case of coating, the gold plasma must first roll up from the cone layer to

the coating layer before entering the fuel layer. Obviously, the greater the gold cone growth rate $\gamma_{12}$, the greater the possibility of gold first entering the fuel layer. As $\gamma_{12}$ has the most severe effect on generating gold plasma rolling-up mixing, we need to prioritize its impact on the overall growth rate of the system. We can see from the three solid lines representing the growth rate $\gamma_{12}$ of the gold cone in the figure that the growth rate gradually decreases with increase in the coating thickness until it increases to the critical saturation thickness, where the growth rate reaches a minimum. The size of the growth rate is no longer reduced with increase in the thickness after that. Therefore, in order to ensure that the interface achieves the minimum KHI growth rate, we can make the coating thickness the same as or slightly greater than the critical saturation thickness.

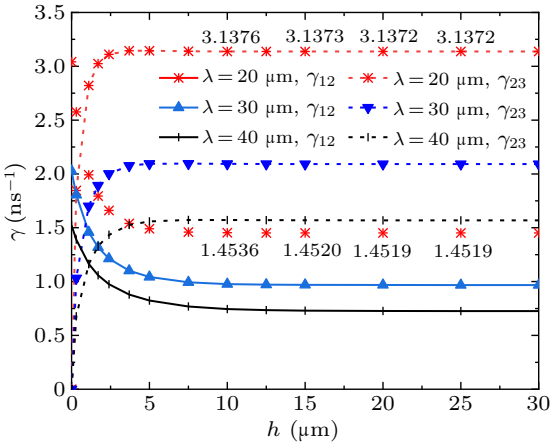



**Fig. 3.** Variation of KHI growth rate with coating thickness at three different perturbation wavelengths.

Regarding the specific value of the critical saturation thickness, we can compare the values of growth rate corresponding to different thicknesses with those corresponding to infinite thickness. Considering the data accuracy of the simulated values, the data given in this paper are only accurate to 0.0001. So when the difference between the two growth rates corresponding to the thickness and the growth rates at infinite thickness does not exceed 0.0001, we regard this thickness as approximately equivalent to infinite thickness, which is the critical saturation thickness we are looking for.

From the chart and the original data, it can be seen that in the case of a wavelength of 20 μm, the thickness $h$ increases from 0 to 15 μm, the growth rate $\gamma_{12}$ gradually decreases to 1.4520 and the growth rate $\gamma_{23}$ becomes 3.1373. After 15 μm all the way to infinity, $\gamma_{12}$ is maintained at 1.4519 and $\gamma_{23}$ is maintained at 3.1372. That is to say, when the thickness reaches 15 μm, the difference between $\gamma_{12}$ and $\gamma_{23}$ and the growth rate at infinity is 0.0001 and 0.0001, respectively. That is, the critical saturation thickness of the coating layer at the perturbation wavelength of 20 μm is 15 μm.

In the case of a wavelength of 30 μm (40 μm), the thickness $h$ increases from 0 to 20 μm (25 μm), and the growth rates $\gamma_{12}$ and $\gamma_{23}$ gradually become 0.9681 (0.7261) and 2.0915 (2.5687), and after 20 μm (25 μm) all the way to infinity $\gamma_{12}$ and $\gamma_{23}$, respectively, remain at 0.9680 (0.7260) and 2.0915 (2.5686). At a thickness of 20 μm (30 μm), the difference between $\gamma_{12}$ and $\gamma_{23}$ and the growth rate at infinity is 0.0001 (0.0001) and 0 (0.0001), respectively. That is, the critical saturated thickness is 20 μm (25 μm).

From the above three data sets, we can generalize that when the wavelength is $\lambda$, the critical saturation thickness is $0.5(\lambda + 10$ μm). We apply this formula to the prediction of the critical saturated thickness at other wavelengths, and eventually find that the actual results are in perfect agreement with the predictions. In addition, we use the same method to verify the relationship between the critical saturated thickness and density and velocity, respectively. The validation results show that the critical saturation thickness is independent of other conditions except the perturbation wavelength.

### 3.3. Efefct of coating density on growth rate

#### 3.3.1. Growth rate under the opposite direction growth effect of interface instability

In the phenomenon of gold–fuel mixing, the gold that should be in the outer cone layer appears in the inner fuel layer. Based on this phenomenon, we can infer that there must exist a problem of the direction of development of the instability in the KHI process. First, according to the theory of fluid mechanics, we know that the direction of KHI should not depend on density. This is because the direction of instability development can be controlled mathematically by changing the sign of the characteristic function. However, our physical intuition from fluid mechanics leads us to believe that the influence of density on the direction of KHI is not just a sign-related mathematical issue but is rather closely linked to the physical mechanisms of fluid dynamics. This remains an important factor in actual physical systems, as it affects the flow characteristics of the fluid and the initial conditions of instability, significantly influencing the formation and development of instability patterns.

Next, we will elaborate on some physical mechanisms derived from actual physical systems. In the mechanism of shear flow, when there is a velocity difference between the upper and lower fluid layers, shear forces can induce instability at the interface. Density differences affect the fluid's acceleration and state of motion, thereby altering the formation of instability patterns. Furthermore, from the perspective of wave modes, the phase velocity and wavelength of waves can differ in fluids of varying densities, which may lead to changes in instability patterns. Specifically, a denser fluid layer may reduce the phase velocity of the waves, thereby affecting the direction of KHI. Energy transfer efficiency between fluids is also dependent on density. Lower-density layers may experience higher gains in wave energy, while denser fluid layers

may dampen wave energy, resulting in different directions of KHI development. Density differences can also give rise to buoyancy effects. In actual fluids, the influence of the gravitational field is present; in denser fluid layers, gravity exerts greater downward pressure, while in less dense fluid layers, buoyancy is relatively stronger. This buoyancy difference can affect the waves at the interface, resulting in different directions of development. This is just a glimpse into the intricate nature of real physical systems. Through these mechanisms, it is evident that there are multiple connections between density and the direction and development of KHI in real physical systems. The interplay of these factors leads to the influence of different fluid layer densities on the direction of KHI. In Subsection 3.3.2, we provide further evidence to support this point. Specifically, in Fig. 10, we offer simulation findings on material content: as the density ratio of the two fluid layers changes, we see different fluid development directions. Therefore, based on the complexity of the mechanisms in actual physical systems, we relate fluid density to the direction of development of KHI. It is necessary to reasonably suppose that the direction of development of the instability is from the high-density gold cone layer to the low-density fuel target layer, which allows the gold plasma to be rolled up into the inner fuel layer due to the instability (see Fig. 4).

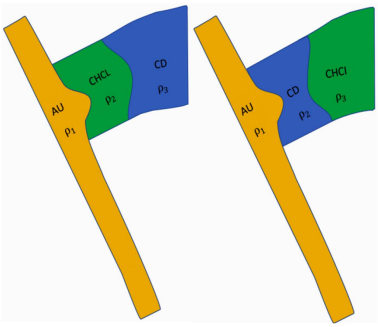



**Fig. 4.** Actual schematic half-cone of the direction of KHI development in the DCI scheme when $\rho_1 > \rho_2 > \rho_3$ (left) and $\rho_1 > \rho_2 < \rho_3$ (right).

From Fig. 4 we can see that when the density of the intermediate coating layer is greater than the density of the target layer, their interlayer instability develops in the same direction as that of the gold cone surface instability (left), which promotes each instability. The opposite happens when the density of the target layer is higher than that of the intermediate coating layer. This causes the interlayer instability to roll up in the opposite direction to the gold cone surface instability (right), inhibiting each instability. We call this phenomenon the opposite direction growth effect of interface instability.

Next, we investigate the effect of different coating densities on the KHI growth rate of the gold cone surface while other conditions remain constant. Since only the coating density $\rho_2$ changes during the coating process, the density of the gold cone layer $\rho_1$ and the target layer density $\rho_3$ are regarded as unchanged. Combining with Eq. (22), for the sake of convenience of representation, we use the change of density ratio $\rho_{23}$ to equate to the change of coating density $\rho_2$. Taking the simulated wavelength as 40 μm, the density conditions are adopted as $\rho_{13} = 15$. We set the speeds to $u_1 = 0$, $u_2 = 20$ μm·ns$^{-1}$, and $u_3 = 40$ μm·ns$^{-1}$ to see how the coating density $\rho_2$ (density ratio $\rho_{23}$) affects the rate of instability growth at three different thicknesses: 5 μm, 10 μm and 20 μm. Due to the large difference in the graphical range of the two growth rates, we plotted them separately in order to improve the visualization.

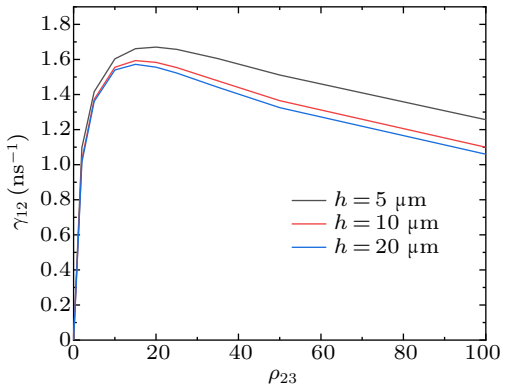



**Fig. 5.** Variation of growth rate between the cone layer and coating with coating density (density ratio $\rho_{23}$) for three different thicknesses.

Firstly, we can see from Fig. 5 that when the coating density $\rho_2$ is less than the gold cone density ($\rho_{23} < 15$), $\gamma_{12}$ increases with increasing coating density and then decreases as coating density increases further. However, from a practical perspective, in Fig. 6 we have only depicted the case where the coating density is less than that of gold, as it is nearly impossible for the coating material used in the actual DCI experiments to have a density higher than the gold cones.

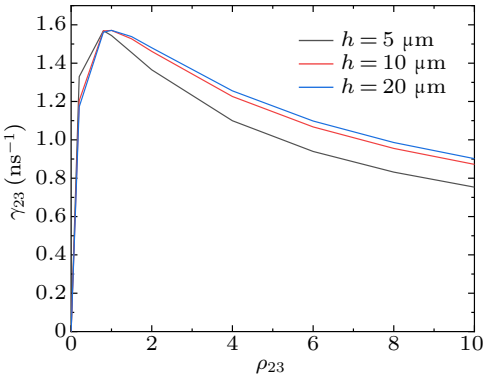



**Fig. 6.** Variation of growth rate between target layer and coating with coating density (density ratio $\rho_{23}$) for three different thicknesses.

Figure 6 shows that, firstly, when $\rho_2 > \rho_3$, the growth rate $\gamma_{23}$ decreases as the coating density $\rho_2$ increases. Combined with the interface effect of rolling up oppositely when $\rho_1 > \rho_2 > \rho_3$ (Fig. 4, left), at this time the KHI development directions of the two interfaces are the same; $\gamma_{23}$ and $\gamma_{12}$ promote each other. So, a larger coating density $\rho_2$ can make the

promoting role of $\gamma_{23}$ smaller, which is beneficial in slowing down the overall growth rate. However, from Fig. 5, we know that $\gamma_{12}$ increases as $\rho_2$ increases. Considering that the premise of this discussion is already $\rho_2 > \rho_3$, hence $\rho_2$ is big enough. Continuing to increase $\rho_2$ will lead to a more serious increase in $\gamma_{12}$. We continue to search for a more optimal solution that can keep the coating density from being too large.

When $\rho_2 < \rho_3$, Fig. 6 shows that the growth rate $\gamma_{23}$ increases with increase in the coating density $\rho_2$. Combined with Fig. 4 (right), it can be seen that at this time, the growth rate of the two interfaces develops in the opposite direction, and $\gamma_{23}$ suppresses and slows the increase of the growth rate $\gamma_{12}$. To get the strongest inverse suppression, the coating density $\rho_2$ can be raised to make $\gamma_{23}$ as big as possible. This lowers the KHI of the system to its weakest level. Moreover, the premise of this discussion is $\rho_2 < \rho_3$. Even if the coating density $\rho_2$ is the largest, it will not cause an ultra-high $\gamma_{12}$ to have a serious effect on the ignition. Due to the opposite weakening of $\gamma_{23}$, this coating density scheme is the optimal scheme we have found to maximally reduce the growth rate of the KHI of the system, i.e., the coating density is slightly smaller than the target layer density.

### 3.3.2. Observing the opposite direction growth effect of interface instability using FLASH simulation

Next, we use FLASH to simulate the cone of Au–CD–CHCl to see if it rolls up the opposite way, which is what our hypothesis of interfacial effects says should happen. The two-dimensional simulation on the $x$–$y$ plane focuses solely on the upper half of the cone, disregarding the lower part for simplicity because of its symmetry. The simulation space is defined by the micrometer coordinates ranging from $(-450, 450)$ on the $x$-axis and $(-100, 600)$ on the $y$-axis. To qualitatively observe the direction of KHI evolution, the simulation employs a grid size of $16 \times 16$ and a grid number of $512 \times 512$. We utilize a downward vertical square wave laser with a duration of 3 ns. The gold cone has a thickness of 30 μm. The CD coating material is deuterated polystyrene with an initial density of 1.0 g·cm$^3$. The actual coating layer is thin, but in order to observe more clearly the changes in the development of fluid instability inside the coating layer we have thickened it to 30 μm, and the target layer CHCl material is chlorinated polyvinyl chloride (CPVC) with a density of 1.5 g·cm$^3$. The inner radius of the target layer fuel is 500 μm and the outer radius is 550 μm.

In order to accurately work out the positional changes of each substance, we used the content of the substance as a percentage plot in the actual observation. Because the unstable flow direction of the gold plasma at the interface of the gold cone is undoubtedly from gold to the internal fuel layer, we only investigated the process at the interface of the coated layer and the target layer. Figures 7–9 show the substance content percentage plots of the coated layer CD and the target layer CHCl at 0 ns (initial moment) and 2.6 ns.

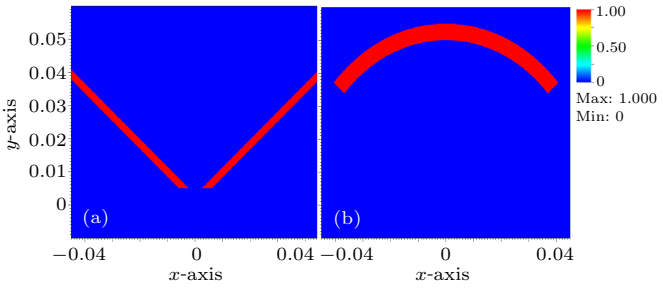



**Fig. 7.** Simulation of the substance content percentage of CD (a) and CHCl (b) at 0 ns.

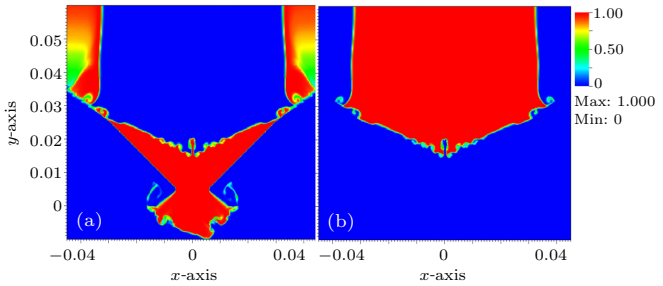



**Fig. 8.** Simulation of the substance content percentage of CD (a) and CHCl (b) at 2.6 ns.

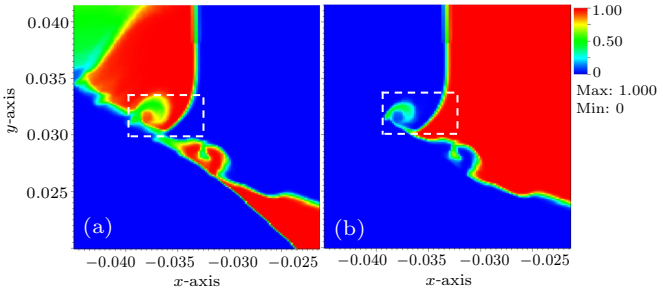



**Fig. 9.** Simulated enlargement plot of the substance content percentage of CD (a) and CHCl (b) at 2.6 ns.

As can be seen from the 2.6 ns zoomed-in image, there are obvious traces of flow development of the CHCl target layer towards the CD coating (area in dotted box), and rolling-up formation is observed near this location. This suggests that opposite rolling-up development indeed occurs when the density of the coating layer is less than that of the target layer.

To be even more sure, we used FLASH to simulate the Au–CHCl–CD model with the density of the target layer being lower than that of the intermediate coating layer (Fig. 10). We then compared this model with the original Au–CD–CHCl model. Unsurprisingly, at the same time, at 2.6 ns, we do observe the development of flow from the high-density coated layer to the low-density target layer (area in solid box). The direction of rolling-up development is different for the two models, but both point from the high-density CHCl layer to the low-density CD layer. This also means that our simulations confirm that the opposite direction growth effect of inter-

face instability does exist, which provides strong support for our theoretical work.

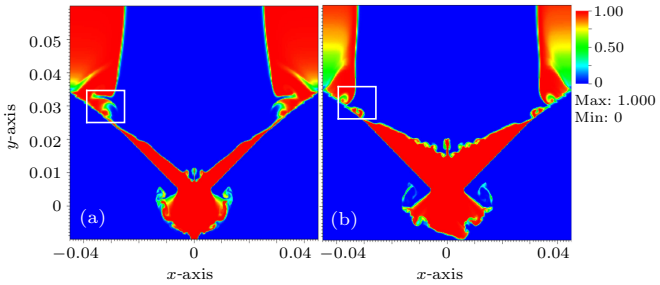



**Fig. 10.** Simulation of the substance content percentage of Au–CHCl–CD coating CHCl (a) and Au–CD–CHCl coating CD (b) at 2.6 ns.

## 4. Conclusion

In this paper, to research the bi-interface KHI between the three fluids of a coated DCI scheme, we use linear theory to derive a quartic equation for the growth rate of the KHI at a bi-interface. From the investigation of the coated thickness, we obtain an empirical formula for the critical saturation thickness $h = 0.5(\lambda + 10\ \mu\text{m})$. When the coating thickness exceeds this critical saturation thickness, the growth rate no longer decreases because of the increase in thickness, so the thickness of the improved coating should be just equal to or slightly greater than the critical saturation thickness. By carefully studying and analyzing the influence of coated density on the KHI of the bi-interface, the opposite direction growth effect of interface instability is proposed. Through this effect, we analyze and conclude that the instability growth rate at the interface of the coated DCI scheme can be minimized by choosing a coating layer with a density slightly smaller than that of the target layer. It is possible to both keep the growth rate on the surface of the gold cone as small as possible and to maximize the suppression of the growth rate of the bi-interface. Finally, the research findings in this work provide some reference for the study of inhibiting KHI in a DCI scheme, particularly regarding the issue of gold mixing.

## Acknowledgment

Project supported by the Strategic Priority Research Program of Chinese Academy of Sciences (Grant No. XDA 25051000).

## References

[1] Lord Kelvin W T 1871 *Phil. Mag.* **42** 362
[2] Helmholtz H V 1868 *Phil. Mag.* **36** 337
[3] Chandrasekhar S 1961 *Hydrodynamic and Hydromagnetic Stability* (London: Oxford University Press) pp. 480–514
[4] Sen A K 1964 *Phys. Fluids* **7** 1293
[5] Michael D H 1955 *Math. Proc. Camb. Phil. Soc.* **51** 528
[6] Sen A K 1963 *Phys. Fluids* **6** 1154
[7] Zhang J, Wang W M, Yang X H, Wu D, Ma Y Y, Jiao J L, Zhang Z, Wu F Y, Yuan X H, Li Y T and Zhu J Q 2020 *Phil. Trans. R. Soc. A* **378** 20200015
[8] Maschke A W 1975 *IEEE Trans. Nucl. Sci.* **22** 1825
[9] Tabak M, Hammer J, Glinsky M E, Kruer W L, Wilks S C, Woodworth J, Campbell E M, Perry M D and Mason R J 1994 *Phys. Plasmas* **1** 1626
[10] Kodama R, Shiraga H, Shigemori K, *et al*. 2002 *Nature* **418** 933
[11] Li J, Davies J R, Ma T, Mori W B, Ren C, Solodov A A, Theobald W and Tonge J 2013 *Phys. Plasmas* **20** 052706
[12] Zhang J, Zhang Z and Wang W M (CN Patent) 111681783 A [2020-09-18]
[13] Henderson D B, McCrory R L and Morse R L 1974 *Phys. Rev. Lett.* **33** 205
[14] Hammel B A, Kilkenny J D, Munro D, Remington B A, Kornblum H N, Perry T S, Phillion D W and Wallace R J 1994 *Phys. Plasmas* **1** 1662
[15] Betti R, Goncharov V N, McCrory R L and Verdon C P 1998 *Phys. Plasmas* **5** 1446
[16] Clark T R and Milchberg H M 1998 *Phys. Rev. E* **57** 3417
[17] Yang H, Zhang J and Li Y 2002 *Phys. Rev. E* **66** 016406
[18] Lindl J D, Amendt P, Berger R T, Glendinning S G, GlenzerS H, Haan S W, KauffmanR L, Landen O L and Suter L J 2004 *Phys. Plasmas* **11** 339
[19] Boozer A H 2005 *Rev. Mod. Phys.* **76** 1071
[20] He X T and Zhang W Y 2007 *Eur. Phys. J. D* **44** 227
[21] Wang L F, Ye W H, Don W S, Sheng Z M, Li Y J and He X T 2010 *Phys. Plasmas* **17** 122308
[22] Betti R and Hurricane O A 2016 *Nat. Phys.* **12** 435
[23] Hill D W and Kingham R J 2018 *Phys. Rev. E* **98** 021201
[24] Duchateau G, Hu S X and Pineau A 2019 *Phys. Rev. E* **100** 033201
[25] Zhang S and Hu S X 2020 *Phys. Rev. Lett.* **125** 105001
[26] Frenje J A 2020 *Plasma Phys. Control. Fusion* **62** 023001
[27] Tao T, Zheng G, Jia Q, Yan R and Zheng J 2023 *High Power Laser Science and Engineering* **11** e41
[28] Zhang Q, Wu F Y, Yang X H, Ma Y Y, Cui Y, Jiang B F and Zhang J 2024 *Phys. Plasmas* **31** 032703
[29] Zhang C L, Zhang Y H, Yuan X H, Zhang Z, Xu M H, Dai Y, Dong Y F, Gu H C, Liu Z D, Zhao X, Li Y T, Li Y J, Zhi J Q and Zhang J 2022 *Chin. Phys. B* **33** 025201
[30] Dai H H, Xu M H, Guo H Y, Li Y J and Zhang J 2022 *Chin. Phys. B* **31** 120401
[31] Li Z, Yang X H, Xu H, Zhang G B, Zeng B, Chen S J, Ma Y Y, Wu F Y and Zhang J 2022 *Phys. Plasmas* **29** 092705
[32] Zhu Z Y, Liu Y X, Li Y J and Zhang J 2022 *Chin. Phys. B* **31** 105202
[33] Fryxell B, Ricker P, Timmes F X, Zingale M, Lamb D Q, MacNeice P, Rosner R, Truran J W and Tufo H 2000 *The Astrophysical Journal Supplement Series* **131** 273